PERGAMON

Chemical Engineering Science 58 (2003) 1615–1629

Chemical Engineering Science

www.elsevier.com/locate/ces

# Time-dependent flow structures and Lagrangian mixing in Rushton-impeller baffled-tank reactor

Marina Campolo, Fabio Sbrizzai, Alfredo Soldati*

*Centro Interdipartimentale di Fluidodinamica e Idraulica and Dipartimento di Scienze e Tecnologie Chimiche, Università di Udine, 33100 Udine, Italy*

Received 5 November 2001; received in revised form 30 November 2001; accepted 3 October 2002

**Abstract**

The object of this work is to investigate the role of large-scale convective structures in promoting mixing in a stirred tank. We focus on a standard geometry (flat bottom, four-baffle reactor stirred by a six-blade Rusthon impeller) and we use an Eulerian–Lagrangian approach to investigate numerically the dispersion of fluid particles. The three-dimensional, time-dependent, fully developed flow field is calculated with a computationally efficient procedure using a RANS solver with $k$–$\varepsilon$ turbulence modeling and the flow field is assessed precisely against experimental data. Then, fluid parcels are tracked in the calculated flow field. Analyzing the trajectory of fluid parcels, the segregated regions within the flow are identified and mixing indicators are calculated (mixing time, circulation length and sojour time distribution). A physical explanation is thus proposed to establish a link between large-scale mixing and complex fluid dynamics generated by the interactions of radial-discharge jet, ring vortices, and upper counter rotating vortex.


*Keywords:* Rushton impeller; Large-scale convective structures; Eulerian–Lagrangian approach; Lagrangian tracking; Mixing

## 1. Introduction

In several industrial processes, mixing is achieved by stirring the fluid contained in a tank with a rotating impeller. The time required to achieve complete mixing is a crucial parameter which can influence the economics of the entire process. Even though it is common perception that the more chaotic is the flow (Lamberto, Alvarez, & Muzzio, 2001) the quicker is mixing, mixing mechanisms are still to be investigated in depth.

Mixing in not easy to define and more complex to measure (Villermaux, 1996; De La Villeon et al., 1998, Delaplace, Leuliet, & Relandeau, 2000; Lamberto et al., 2001). In a stirred tank reactor, mixing is driven by impeller-generated convective motion at larger scales, by turbulent transfer at smaller scales, down to diffusion to molecular scales (Nagata, 1975). In this work, we propose to calculate numerically the time-dependent flow field in a stirred tank reactor and to use Lagrangian particle tracking to investigate mixing related phenomena. Lagrangian tracking coupled to a time-dependent Eulerian solution of the flow field ensure proper modeling of the time evolution of mixing structures (Houcine, Vivier, Plasari, David, & Villermaux, 1996; Distelhoff & Marquis, 2000; Guillard, Trägårdh, & Fuchs, 2000).

Lagrangian experimental analyses have been performed by Hill, Sharp, and Adrian (2000) using particle image velocimetry (PIV), by Houcine et al. (1996), Guillard et al. (2000) and Hill et al. (2000) using plane laser induced fluorescence (PLIF), by Rammohan, Kemoun, Al-Dahhan, and Dudukovic (2001) using computer automated radioactive particle tracking (CARPT) and by Fangary, Barigou, Seville, and Parker (2000) using positron emission particle tracking (PEPT). Lagrangian numerical analyses have been performed by De La Villeon et al. (1998), Harvey III, West, and Tufillaro (2000), and Lamberto et al. (2001). The advantage of Lagrangian methods is that the physics of dispersion and mixing appears clearly. Their numerical downside is the heavy computational requirement for tracking large numbers of particles. Given the intermittent nature of the mixing process, this is to be coupled to the heavy requirement to compute the three-dimensional, time-dependent Eulerian flow field necessary to time-trace mixing.

* Corresponding author. Tel.: +39-0-432-558864; fax: +39-0-432-558803.
*E-mail address:* soldati@uniud.it (A. Soldati).
*URL:* http://158.110.50.22

0009-2509/03/$ - see front matter © 2003 Elsevier Science Ltd. All rights reserved.
doi:10.1016/S0009-2509(02)00658-9

Less demanding, Eulerian–Eulerian methods are also applied (Patwardhan & Joshi, 1999; Sahu, Kumar, Patwardhan, & Joshi, 1999; Brucato, Ciofalo, Grisafi, & Tocco, 2000; Patwardhan, 2001), even though they are not as plentiful of information as Lagrangian approaches.

In this work, we chose to investigate mixing in the standard reactor examined by Yianneskis, Popiolek, and Whitelaw (1987). The three-dimensional, time-dependent, fully developed flow field is calculated adopting a sliding mesh approach to reproduce the effect of impeller rotation at best. We show that the computational cost of the flow field calculation can be reduced adopting a "hybrid" approach (Harvey & Rogers, 1996), which exploits an approximate steady-state solution for the initialization rather than the condition of still fluid (Serra, Campolo, & Soldati, 2001; Campolo, Paglianti, & Soldati, 2002b; Campolo & Soldati, 2002). The computed flow field is validated against data by Yianneskis et al. (1987), by Wu and Patterson (1989), by Michelet, Kemoun, Mallet, and Mahouast (1997) and by Kemoun, Lusseyran, Mallet, and Mahouast (1998). Then, fluid parcels are tracked to build a Lagrangian database for dispersion. This database is used to calculate (i) circulation time and circulation length distributions (Villermaux, 1996) and (ii) a map for the sojour time distribution (Rammohan et al., 2001). Finally, an explanation is proposed to justify the mixing differences observed in the upper part of the tank compared to the lower part of the tank.

## 2. Methodology

### 2.1. Problem geometry

We focus the analysis on the reactor investigated by Yianneskis et al. (1987), the geometry of which is shown in Fig. 1(a). The reactor is a cylindrical vessel of diameter $T = 294$ mm, filled with water up to $H = T$. The fluid is stirred by a standard six-blade Rushton turbine (diameter $D = T/3$, blade height $W = D/5$, blade width $D/4$), and the tank is equipped with four baffles (width $T/10$).

The numerical simulation considers the impeller clearance, $C$, fixed at $T/3$ and the angular velocity, $\Omega$, equal to 300 rpm. Conditions examined correspond to a Reynolds number ($Re = \rho N D^2/\mu$) equal to 48,020, i.e. fully turbulent flow (Nagata, 1975).

### 2.2. Numerical methodology

The three-dimensional, time-dependent flow field is calculated using a finite-volume solver (StarCD®). The computational domain, corresponding to the volume of fluid in the tank discretized into finite volumes, is shown in Fig. 1(b). For grid assessment purposes, we considered three different finite-volume discretizations (174,980, 377,432 and 450,006 finite volumes), corresponding to a coarse mesh, a fine mesh (the one shown in Fig. 1(b)) and a very fine mesh model.

The code solves for the balance equations of mass and momentum in the Reynolds averaged form. Boundary conditions are no slip at solid surfaces (wall and impeller) and no shear at the flat free surface corresponding to the upper air–water interface. Since the flow is turbulent, a $k$–$\varepsilon$ model complemented by the algebraic "law of the wall" is employed to reproduce the flow up to the near-wall regions. This model for turbulence limits the computational cost of the simulations and achieves accurate results for the flow field, provided that the grid is sufficiently refined (Ranade, Joshi, & Marathe, 1989; Bartels, Breuer, & Durst, 2000).

The effect of the impeller rotation is reproduced adopting the sliding mesh approach (SMA) which divides the computational domain in two regions—(i) a cylindrical region containing the impeller and (ii) the rest of the tank—and solves the balance equations in a rotating frame of reference in region (i) and in a fixed frame of reference in region (ii). Information exchanged between the static and the rotating regions through the sliding interface accounts for the changing relative position after each time iteration.

We chose to characterize the mixing process with reference to pseudo-steady state, in which the statistics of flow variables show a time dependence which is a straightforward function of the blade frequency. This condition can be easily reproduced by experiments and corresponds to the real working condition for continuously fed stirred tanks. In the real apparatus, the pseudo-steady state is achieved after a large number (order 30) of impeller revolutions starting from fluid at rest. To avoid the numerical calculation of the initial transient of agitation, the simulation starts from an initial condition alternative to the fluid at rest (Harvey & Rogers, 1996). The divergence free flow field is calculated using a multiple frame of reference (MFR) approach (Luo, Issa, & Gosman, 1994), which solves the balance equations by a steady state algorithm, considering the position of the static and the rotating region of the computational domain fixed. This solution, obtained at low cost, cannot be used to analyze the intrinsically dynamic, impeller-driven, mixing structures and yet is a sub-optimal starting condition for the full transient SMA simulation of the pseudo-steady state. We named "hybrid" approach the strategy that starts from the MFR field and continues with the SMA computations.

### 2.3. Computational cost and accuracy of hybrid approach

Accuracy and cost of the hybrid versus the full sliding mesh approach are evaluated performing two numerical simulations on the coarse mesh, as shown in Table 1. The first simulation is a full transient, sliding mesh simulation from fluid at rest to pseudo-steady state. The second simulation is the MFR simulation necessary to obtain the starting flow field, followed by the SMA for the number of revolutions necessary to achieve a fully developed flow field.

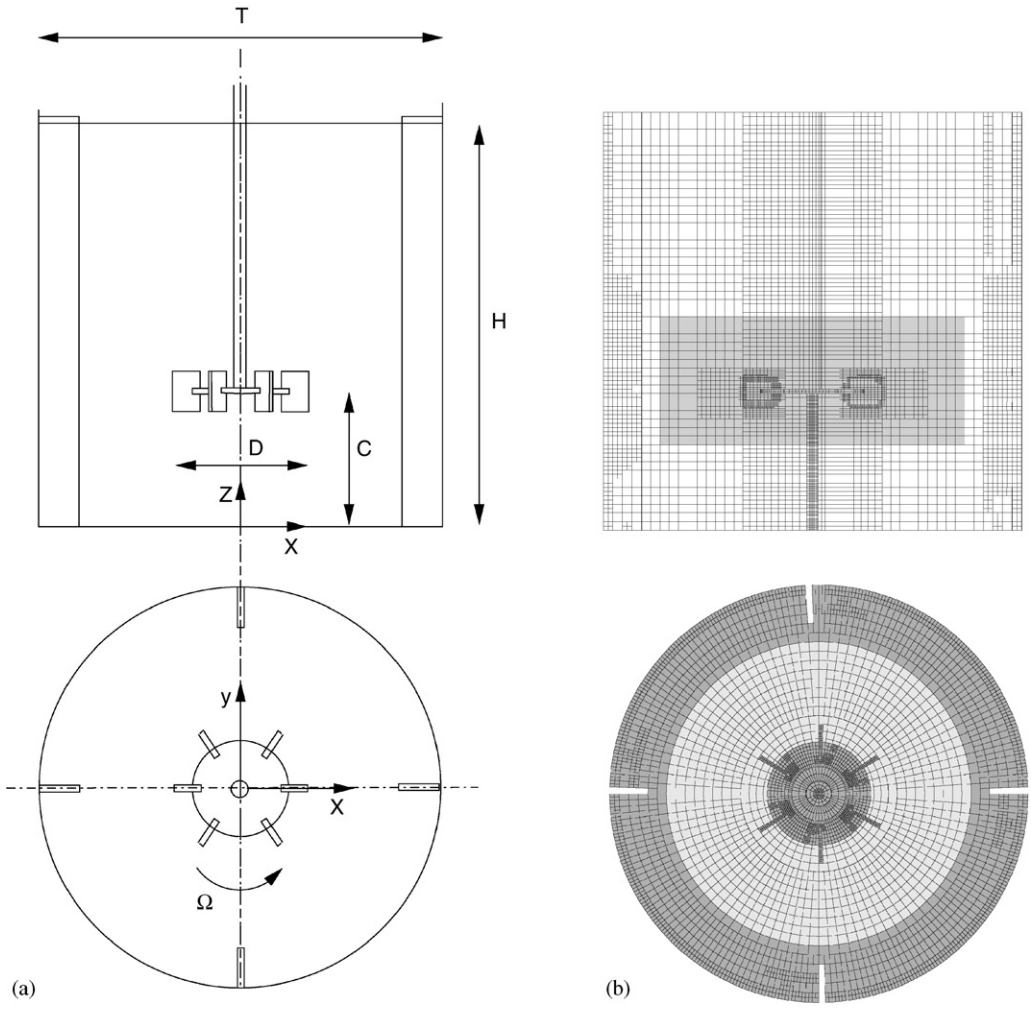


Fig. 1. Standard configuration for stirred tank equipped with Rushton impeller (Yianneskis, Popiolek, and Whitelaw, 1987) (a), and fine mesh model (about 377,000 finite volumes) (b). Grid is adaptively refined in large velocity gradient regions.

Table 1
Computational costs associated to full sliding mesh (SMA) and hybrid (MFR + SMA) approaches for calculation of three dimensional, fully developed flow field

| Approach | No. of iterations ($S_{MFR}$ = steady, $T_{SMA}$ = transient) | CPU time[a] |
|---|---|---|
| Full sliding mesh | 4000 $T_{SMA}$ | 191 min 42 s |
| Hybrid | 346 $S_{MFR}$ + 1000 $T_{SMA}$ | 59 min 26 s |

[a]Calculated on 2 × 400 MHz processor, 1 Gb RAM server.

Convergence toward pseudo-steady state is verified monitoring over time—i.e. for an increasing number of impeller revolutions—power input and kinetic energy variation. Power input variation is strictly related to the complex three-dimensional turbulent flow field developing in the vessel, particularly in the vicinity of the impeller. Kinetic energy variation accounts for modification of the structure of the flow in the entire vessel.

In Fig. 2(a), we show the time behavior of power input, $P$, calculated as the torque on impeller blades and shaft times the angular velocity (Harvey & Rogers, 1996):

$$P = \boldsymbol{\omega} \cdot \int_A \mathbf{r} \times (\boldsymbol{\tau} \cdot \mathrm{d}\mathbf{A}), \tag{1}$$

where, $A$ is the surface of impeller and shaft, $\boldsymbol{\omega}$ is the angular velocity vector (RPS), $\mathbf{r}$ is the position vector, $\boldsymbol{\tau}$ is the stress tensor, and $\mathrm{d}\mathbf{A}$ is the differential surface vector. The solid line and the line with symbols represent values corresponding to the full sliding mesh simulation and to the hybrid approach, respectively. We discussed about the variation of power input from the starting condition of still fluid to fully developed conditions in Campolo et al. (2002b), observing that stationary power input indicates that the flow field is in pseudo-steady state.

From Fig. 2(a), we observe that, if SMA is used starting from fluid at rest, 20 impeller revolutions are necessary to obtain a steady power input. If SMA is used starting from the MFR flow field, 2 impeller revolutions are necessary

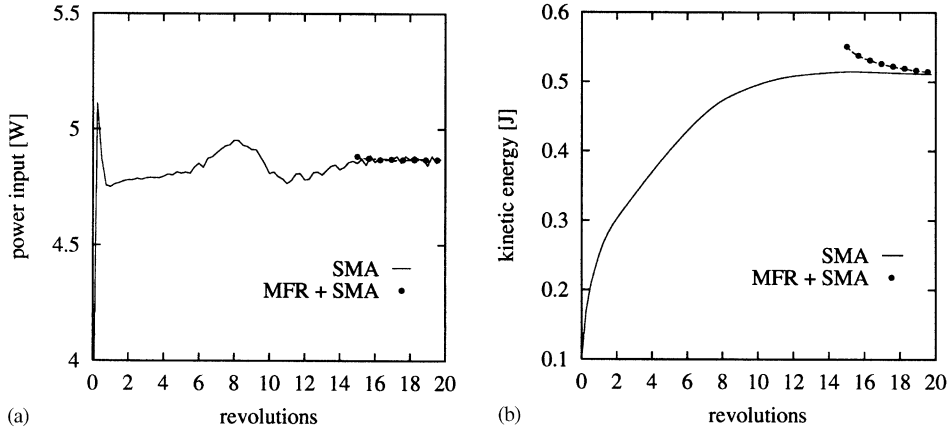


Fig. 2. Convergence to pseudo-steady state: evolution of power input (a), and fluid kinetic energy (b) for the full sliding mesh (SMA) and the hybrid (MFR + SMA) approaches.

to obtain a steady power input. However, we need a further indication to decide whether the pseudo-steady state is obtained or not. We thus monitored over time, the volume integral of the fluid kinetic energy, $E_k$, calculated as

$$E_k = \int_V \rho \frac{v^2}{2} \, \mathrm{d}V, \tag{2}$$

where, $V$ is the volume of fluid in the vessel. Kinetic energy varies steeply at the beginning of agitation and gradually becomes steady when pseudo-steady state is achieved. From Fig. 2(b), we observe that this is attained after 20 impeller revolutions starting from fluid at rest, and after 5 impeller revolutions starting from the MFR flow field. We evaluated that the maximum difference between local values of velocity calculated by the MFR and the SMA, normalized to the blade tip velocity ($v_{\mathrm{tip}} = 1.54$ m/s), is 15% at the beginning of the hybrid calculation and is 2% after 5 SMA revolutions, indicating that the accuracy of the "hybrid" approach is the same of the full SMA.

In Table 1, the computational costs of the two simulations are compared. The MFR solution was obtained in 346 iterations. For the SMA, we ran trial simulations aimed at verifying the influence of time step on accuracy and convergence rate and we found an optimal time step of $\Delta t = 0.001$ s, i.e. each complete impeller revolution with the SMA requires 200 iterations. Each iteration requires about 2.6 s of CPU time on a $2 \times 400$ MHz processor, 1 Gb RAM server. Since transient iterations (SMA) or steady iterations (MFR) require the same time, computation time depends directly on the total number of iterations, so that the procedure MFR followed by SMA reduces the overall CPU time to about 33% of the full sliding mesh procedure.

### 2.4. Grid sensitivity and flow field validation

Simulations were performed on the coarse, fine and very fine models. The solution obtained for the fine grid model (377,432 finite volumes) differs for less than 2%, normalized by the blade tip velocity, from that on the very fine mesh (450,006 finite volumes). Details about the grid-independence analysis may be found in Appendix A.

The flow field was accurately validated against previous experiments (Yianneskis et al., 1987; Wu & Patterson, 1989; Michelet et al., 1997; Kemoun et al., 1998). Details are reported in Appendix A.

## 3. Results

### 3.1. Lagrangian tracking

We calculated the trajectories of tracer particles integrating the kinematic equation of motion,

$$\frac{\mathrm{d}\mathbf{x}_p}{\mathrm{d}t} = \mathbf{v}_p, \tag{3}$$

where, $t$ is time and $\mathbf{x}_p$ and $\mathbf{v}_p$ are fluid parcel position and velocity, respectively. To integrate Eq. (3) over time, the velocity of the fluid must be calculated at each particle position. We used the particle location algorithm developed by Zhou and Leschziner (1999) to identify the four nearest computational nodes around the particle and then we interpolated linearly these values of velocity at the particle position. We used the flow field data calculated with the fine mesh model, describing the flow field evolution corresponding to four impeller revolutions. The time resolution for the flow field is 0.001 s, corresponding to 1.8° of discrete rotation of the sliding mesh.

Even though the flow field is time-dependent, turbulent fluctuations at scales smaller than the grid size are filtered out and this may affect mixing evaluation. Several methods are available to reintroduce the effect of small-scale turbulence on particle trajectories (Gosman & Ioannides, 1981; Graham & James, 1996; Campolo, Fornasier, & Soldati, 2002a). Most of them exploit calculated turbulent kinetic energy and dissipation rate distributions to reconstruct turbulent fluctuations of the velocity field. These

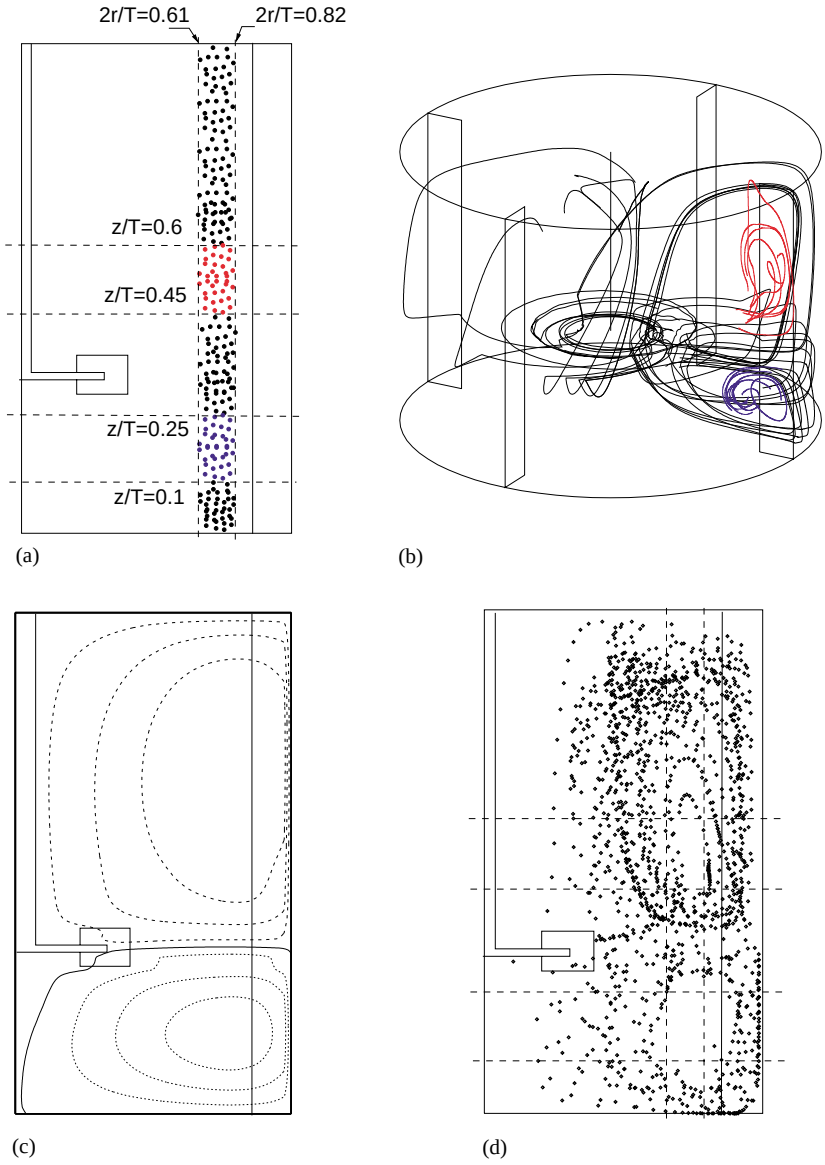


Fig. 3. Particles tracking results: (a) initial distribution of particles, (b) trajectories calculated for particles released in impeller stream jet (black line), in upper circulation eye (red lines) and in lower circulation eye (blue lines); (c) streamlines in vertical section of vessel; (d) radial and vertical positions visited by black particles during simulated period (4 impeller revolutions).

turbulent quantities cannot be assessed precisely against experimental data which rarely allow a complete characterization of turbulence in the different regions of the tank (see, for instance, Magni, Costes, Bertrand, & Couderc, 1990; Mavros, Xuereb, & Bertrand, 1998). Furthermore, there is no clear consensus even on experimental measurements. For example, RMS of velocity fluctuations in the radial, tangential and axial direction are reported to be up to 100%, 180% and 144%, in the impeller stream and up to 155%, 222% and 176% in the bulk of the flow in the paper by Magni et al. (1990). Papers by Wu and Patterson (1989), Kresta and Wood (1993), Lee and Yianneskis (1998) and Wernersson and Trägårdh (2000) indicate that the intensity of turbulent fluctuations in the radial, angular and vertical directions may be up to 50% of the blade tip velocity in the impeller stream region, whereas in the bulk of the flow values are lower (about 10%). These measurements, though confirming the important role of turbulence on transport, do not allow a precise reconstruction of turbulence effects. Therefore, basing also on previous literature indicating that large-scale, convective transport controls the process (Patwardhan & Joshi, 1999; Patwardhan, 2001), we decided to neglect the effect of these small scales.

Eq. (3) was integrated using a time step equal to $2.4 \times 10^{-5}$ s. This time step is sufficiently small to meet the Courant–Friedrichs–Levy condition (Kemoun et al., 1998) and to follow accurately curved trajectories. Particle swarms are then tracked storing particle data every 0.001 s,

i.e. the same time step used to update the time-dependent flow field and the position of the moving part of the grid.

### 3.2. Tracer trajectories and identification of segregated regions

Trajectories of tracers in the tank depend strongly on their starting position. We performed a numerical experiment following a group of 3000 fluid particles injected at random positions in a very thin cylindrical sector extending from the free surface to the bottom of the tank ($2r/T = [0.61 : 0.82]$, $\theta = [-2° : 2°]$ and $z/T = [0.01 : 0.98]$), as shown in Fig. 3(a). When particles are injected, the sector, the blade and the baffle are aligned in the same angular position. Following the trajectories of the particles, three main types of trajectories are identified (see Fig. 3(b)): black trajectories, followed by particles wandering in the entire vessel; red trajectories, followed by particles confined in the upper part of the vessel; blue trajectories, followed by particles confined in the lower part of the vessel. Tracking backwards the trajectories, we were able to identify the starting position of the three groups, shown in Fig. 3(a) using the same color-code. In particular, blue particles are released at $z/T = 0.1–0.25$ and red particles are released at $z/T = 0.45–0.60$. The different behavior of the particles belonging to the three groups can be explained observing Fig. 3(c), where the streamlines in a vertical cross-section of the tank are shown. The horizontal streamline, corresponding to the radial discharge jet, completely separates the region above and below the impeller. As shown in Fig. 3(b), particles injected above the impeller mid-plane circulate in the upper part of the tank, whereas particles injected below the impeller mid-plane circulate in the lower part of the tank. Closed streamlines above and below the radial jet correspond to the upper and lower ring vortices.

From Fig. 3(b), we observe also that particles driven by the impeller jet seem to avoid specific regions during their upward-downward motion. To identify these regions, we considered a vertical section of the tank, as shown in Fig. 3(d), and we examined particle trajectories in terms of radial and vertical coordinates. Random-sampling over time the trajectory of particles driven by the impeller jet, we marked with a dot their radial and vertical position in the tank, as shown in Fig. 3(d). For clarity of presentation, we show only 2000 random positions. We observe that the large-scale circulation avoids two flow regions corresponding to the cores of lower and upper ring vortices (see Fig. 3(c) and Table 2 in Appendix A). Therefore, a clearcut separation exists between tracers driven into motion by the impeller and tracers entrained and segregated in the ring vortex cores, well in agreement with results presented by Lamberto et al. (2001), who examined mixing in an unbaffled tank equipped with a Rusthon impeller by means of Poincarè maps. They were able to identify toroidal segregated regions in which particles remain indefinitely. Furthermore, they found that stretching of fluid elements increases linearly in these segregated regions, and exponentially in the bulk of the flow. As shown in Fig. 3(b), we notice that red and blue particles within the segregated regions travel only short distance about their initial position, and that they do not spread in the angular direction.

Table 2
Quantitative comparison between simulation results (fine mesh model) and Yianneskis et al. (1987) data

| Variable | Yianneskis et al. (1987) | Present work |
|---|---|---|
| Centre of circulation | $(0.30, 0.20)_{\text{lower}}$ | $(0.29, 0.19)$ |
| $(r/T, z/T)$ (m, m) | $(0.30, 0.48)_{\text{upper}}$ | $(0.29, 0.49)$ |
| Discharge flow angle | 4° | 4.5° |
| Power number | 4.8 | 4.2 |
| Max kinetic energy ($m^2/s^2$) | 0.4 | 0.26 |
| Max dissipation rate ($m^2/s^3$) | 25. | 69. |

### 3.3. Mixing time

Mixing time and circulation time are two criteria used to characterize large-scale mixing (Delaplace et al., 2000). Mixing time is the time required to achieve a certain degree of homogeneity. Circulation time is the time necessary for a fluid element to circulate over a reference distance. The link between these two parameters is clear: the lower the time for particles to circulate in the tank, the more efficient is mixing. In common practice, mixing time is usually taken equal to some multiple of the circulation time to account for the quasi-random paths of the flow (Patwardhan & Joshi, 1999), whereas the circulation time is evaluated as the ratio between the circulation path length divided by the circulation velocity (McManamey, 1980; Joshi, Pandit, & Sharma, 1982).

In this work, since the flow is three dimensional, a circulation path may not be defined as a closed trajectory. Rather, the circulation path is defined fixing a reference surface within the tank (Villermaux, 1996), and considering the trajectory of the particle with respect to this surface. In Fig. 4, we show two schematic and yet representative particle trajectories. Particle A is initially in the impeller stream jet and circulates along the lower ring vortex, and particle B circulates in the core of the lower ring vortex. The cylindrical surface, $S$, to calculate the circulation paths is chosen precisely at $2r/T = 0.738$, is coaxial to the shaft and crosses the core of lower and upper ring vortices. Along each particle trajectory, the points in which particles cross the surface $S$ being directed outward (point 1), inward (point 2), and again outward (point 3), are identified. The part of the trajectory between point 1 and 3 is the circulation path.

For each circulation path identified in the particle database, we calculated (i) the length, $L_c$, and (ii) the circulation time, $T_c$. The length of the circulation path is necessary to calculate the time of circulation, and gives informations about spatial lengthscales of mixing. The

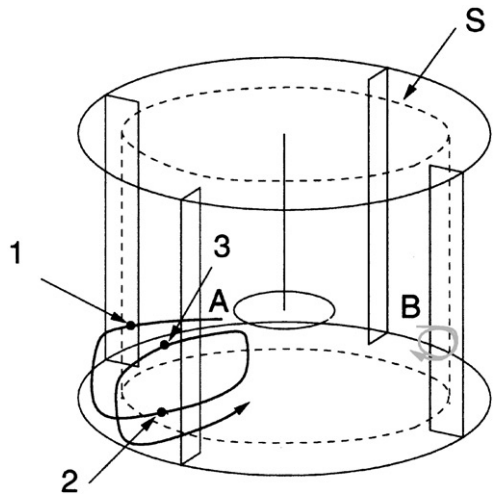


Fig. 4. Sketch for circulation time calculation: each circulation loop is defined with reference to surface $S$, which crosses the segregated regions.

shorter the circulation path, the smaller the region where convective mixing takes place. The frequency distributions of circulation length and time are shown in Fig. 5(a) and (b), respectively.

The frequency distribution of the circulation length (Fig. 5(a)) is bi-modal, with two peaks. The mean value of $L_c$ in the distribution is 0.253 m, lower than the tank diameter, the usual reference lengthscale for convective mixing (Fangary et al., 2000). The frequency distribution is highly nonuniform, with a circulation length less than 0.1 for a fraction of tracers equal to 11%, indicating that these tracers circulate over very short distances, whereas 40% of the tracers wander over distances larger than the reference lengthscale.

The observed frequency distribution can be explained following a physical argument. A correlation between circulation lengths and starting position of particles exists and suggests that: (i) $L_c$ is less than 0.1 for particles released into the core of the upper and the lower vortices, (ii) $L_c$ is in the range 0.1–0.3 for particles released in the impeller stream jet and following the lower ring vortex, and (iii) $L_c$ is larger than 0.3 for particles following the upper ring vortex. As shown in Fig. 3(c), the shortest closed streamlines correspond to vortex core regions, their size increases in the lower part of the tank and reach the maximum in the upper part of the vessel. Experimental observations (Lamberto, Alvarez, & Muzzio, 1999) confirm that tracers released in the vortex core regions circulate confined in a small volume of fluid.

The frequency distribution of the circulation time, $T_c$, is shown in Fig. 5(b). The curve is, again, bi-modal with two main peaks, and characterized by a mean value equal to $T_c = 2.0$ s. Distribution is quasi-symmetric, with half (56%) of tracers characterized by circulation times lower than the mean. Cross-correlation between particle circulation time and particle starting position shows that: (i) particles following the lower vortex circulate with time $T_{c,1} = 1.26$ s; (ii) particles following the upper vortex circulate with time $T_{c,2} = 1.46$ s; and (iii) particles moving with small velocity in the segregated regions circulate with time $T_{c,3} \simeq 3$ s. It is therefore apparent that, if we characterize mixing with the mean value of the circulation time we can give only an oversimplified, nonrepresentative description of the complex development of mixing in the tank. Similar results have been found in experiments where, changing the injection point for tracers, different mixing times are measured (Patwardhan & Joshi, 1999).

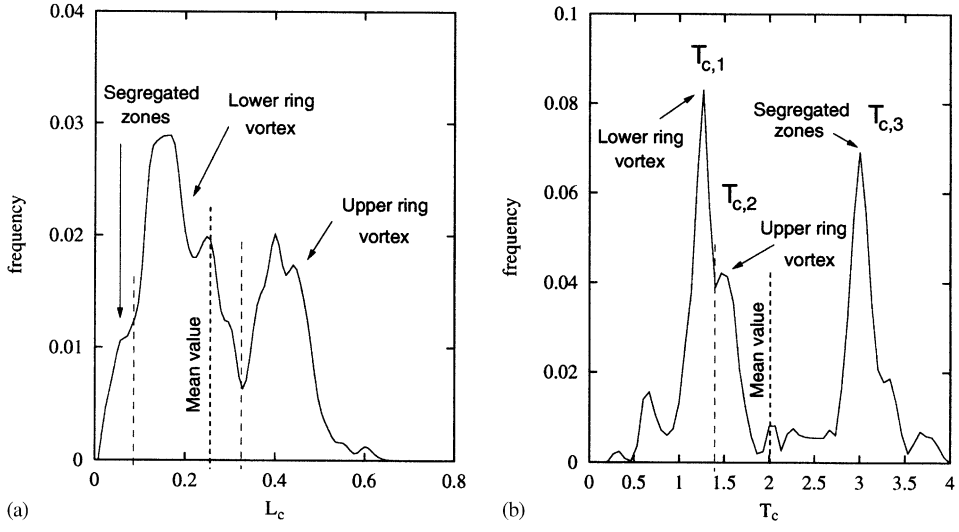


Fig. 5. Circulation length (a) and circulation time (b) frequency distribution calculated from Lagrangian database.

Frequency distributions of circulation time are therefore crucial for a precise investigation of mixing. However, for practical engineering applications, a single value of mixing time is usually calculated exploiting correlation models based on impeller geometric parameters and rotation velocity. Following Holmes, Voncken, and Dekker, (1964), the frequency of circulation, i.e. the inverse of circulation time, for $Re > 2 \times 10^4$ can be predicted as

$$f = 1.12N \left(\frac{D}{T}\right)^2, \quad (4)$$

where, $T$ is the height of the tank. This gives a $T_{c,\mathrm{ave}} = 1/f = 1.61$ s, which is in good agreement with the mean value calculated from the frequency distribution.

### 3.4. Sojour time distribution

Analyses of tracer trajectories and mixing time indicate that mixing is not homogeneous in the tank. In this part of the paper, we try to quantify such nonhomogeneity using the distribution of sojour time for tracer particles in the different regions of the tank.

Sojour time is inversely related to tracer velocity. Particles circulating fast spend short time in each position and visit different regions of the tank, whereas particles circulating slowly spend long time in small neighborhoods.

The residence time for tracers is calculated following the approach proposed by Rammohan et al. (2001). The analysis is restricted to a vertical tank section divided in a regular matrix of cells. Considering the trajectory of a particle in terms of radial and vertical coordinates, (i) the cell containing the particle is identified for each time step, and (ii) the particle residence time in the cell is measured. Considering that trajectories for 3000 particles are simulated, for each cell we obtain a residence time distribution which may be considered statistically steady. In Fig. 6, the mean residence time in the vertical tank section is shown. The three-dimensional surface gives a pictorial representation of the residence time variation, whereas iso-contours can be used for a more detailed examination. The surface is characterized by an elongated canyon in the impeller region (A), two main peaks located near the wall of the tank, one above (B) and one below (C) the impeller mid-plane, and three other smaller peaks (D, E and F). The two peaks, identified with the letters B and C, correspond to the cores of the upper vortex and of the lower vortex, where particles circulate over short distances with large circulation times. Apparently, the two peaks, identified with the letters D and E, are corner-like situations. The peak, identified with the letter F, is generated by the complex, three-dimensional fluid pattern occurring downstream the baffle (Serra et al., 2001). The five peaks correspond to high residence time regions and indicate that injected tracers remain in the same position for a long time, preventing an effective convective mixing. The residence time iso-contours correspond to 0.01 and 0.02 s (solid lines), 0.04, 0.06 and 0.08 s (dashed lines), and 0.10, 0.12 s (dotted lines) and are used to examine the nonhomogeneity of mixing from a quantitative viewpoint. Sojour time values 10 times larger than in the impeller stream are found for the ring vortex cores, where tracers move slowly in the radial, axial and azimuthal directions, have few escape-ways and remain trapped into small-scale circulations indefinitely. Interestingly, we find a large sojour time in the region where the discharge jet impinges the wall of the tank—impeller impingement zone, generating a stagnation point.

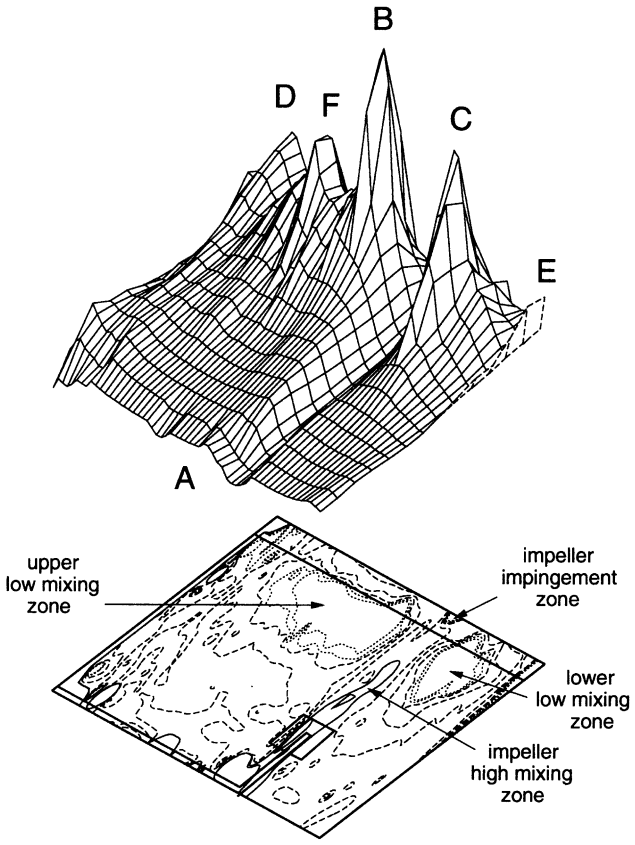


Fig. 6. Mean sojour time distribution (STD) of tracer in tank. Contour values are equal to 0.01 and 0.02 s (solid lines), 0.04, 0.06 and 0.08 s (dashed lines), and 0.10, 0.12 s (dotted lines). Higher STD values correspond to low mixing zones.

### 3.5. Analysis of mixing in lower and upper vortices

The object of this section is to examine the behavior of those tracers injected in the impeller driven stream. Specifically, we focus on the different dispersion observed in the lower and in the upper part of the tank. A new numerical experiment was thus planned to examine the behavior of 3000 particles injected in the impeller stream region only, i.e. $2x/T = [0.3–0.6]$, $y/T = [-0.02–0.02]$ and $z/T = [0.24–0.44]$. In Fig. 7, we show the time trajectory of particles tracked using 12 snapshots taken at 0.05 s intervals, covering the first three revolutions. We show only 150 random-chosen particles for the sake of clarity. Soon after release,

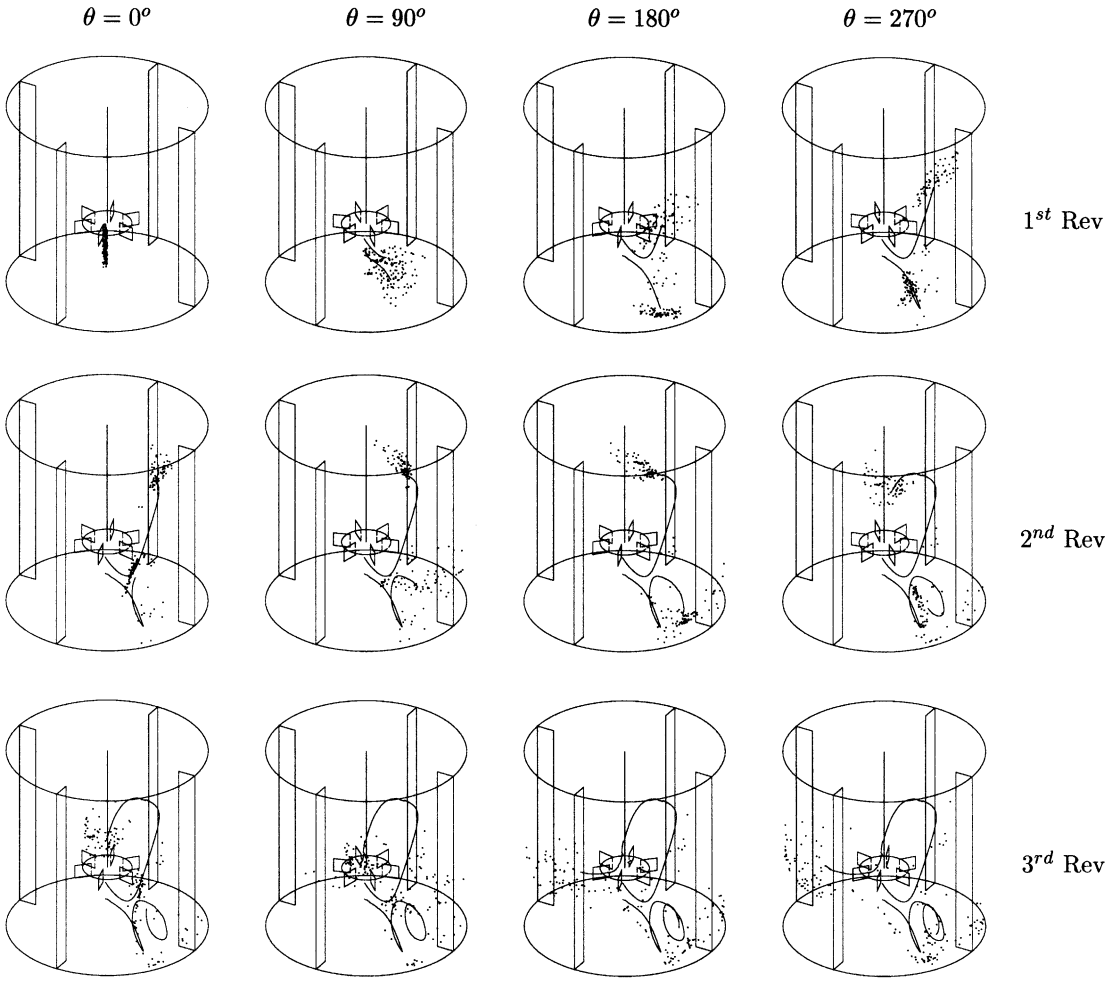


Fig. 7. Lagrangian evolution of fluid tracers released in discharge stream jet. Snapshots cover three impeller revolutions and images are taken at 0.05 s intervals.

particles disperse uniformly driven by the impeller stream (1st revolution, $\theta = 90°$). Afterwards, particles initially located above and below the impeller plane follow different trajectories. The particles initially located above the impeller plane are entrained by the upward moving branch of the blade jet, whereas the particles initially located under the impeller plane are entrained by the downward moving branch of the blade jet. Along with the instantaneous position of each particle, we plotted the entire path history of the center of mass of the upward directed and downward directed swarms of particles.

Consider first the swarm going downward. Particles move coherently toward the bottom of the tank and already entirely cover the path along the lower ring vortex during the first impeller revolution (2nd revolution, $\theta = 0°$). Such active stirring, however, does not correspond to efficient dispersion. During the third impeller revolution, even though the center of mass of the swarm has already performed almost three circulations around the lower ring vortex, particle dispersion is limited to the region close to the first baffle, with 50% already having transpassed the baffle. The scarce dispersion is due to the essentially two dimensional structure of the lower ring vortex. Particles entrained by this vortex have few escape-ways from the vortex path-lines.

Consider now the swarm of particles entrained by the upper ring vortex. The velocity in this vortex is lower and particles reach the upper part of the vessel moving slowly in the vertical direction. In the second snapshot ($\theta = 90°$) of the second impeller revolution, particles start moving inward towards the impeller shaft and immediately also acquire a clockwise motion in the horizontal plane which is opposite to the impeller rotation. This motion is due to the large-scale vortex near to the shaft rotating in the opposite direction with respect to the impeller. This vortex, which was observed previously by Yianneskis et al. (1987), is a complex three-dimensional structure generated by the interaction between the upper ring vortex and the free surface. We believe this structure responsible for the larger dispersion of particles observed above the impeller plane. We identified the extension of the counter rotating vortex considering the axial component of the vorticity in a vertical section of the tank through the axis, as shown in Fig. 8(a). The snapshot is

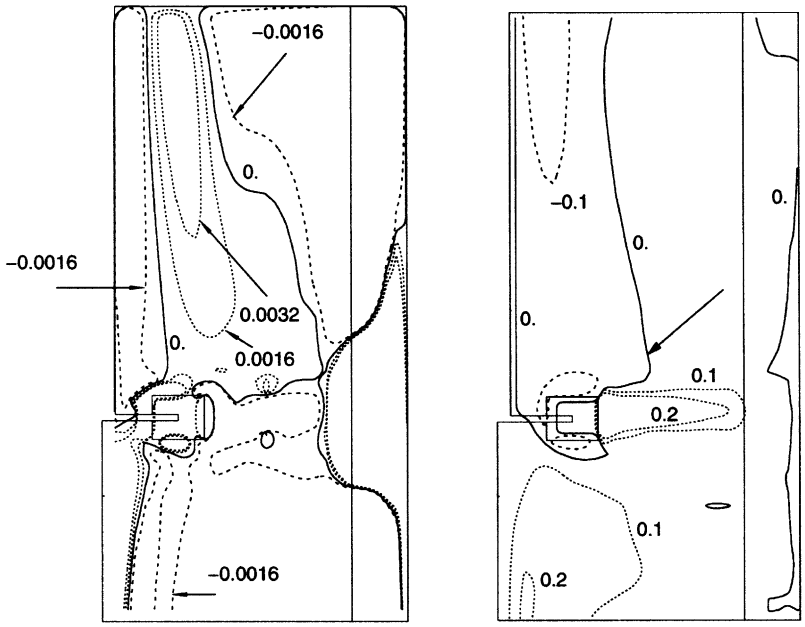


Fig. 8. Snapshot of (a) axial vorticity and (b) azimuthal velocity in vertical section of tank when one impeller blade is aligned to one baffle.

taken when an impeller blade is aligned with one baffle, i.e. corresponding to $\theta = 180°$ 2nd revolution. Axial vorticity is negative near the rotation axis, changes to positive, and then again to negative going toward the vessel wall. We used also azimuthal velocity to identify the inner vortex. In Fig. 8(b), the azimuthal component of velocity is shown for the same section of Fig. 8(a). The impeller rotates counter-clockwise ($v_\theta > 0$) yet the baffles and the free shear upper boundary condition generate the one central clockwise rotating vortex characterized by $v_\theta < 0$ (Yianneskis et al., 1987). The variation in azimuthal velocity which is found in this region is relevant for particle dispersion. Moreover, it is concentrated in a short radial distance, i.e. the rate of change of azimuthal velocity is large and the strain is large. Observing the motion of particles in the third revolution (see Fig. 7), we can suggest that particle dispersion increases sharply when crossing the high strain region between the inner clockwise rotating vortex and the outer flow moving counter-clockwise.

To verify these assumptions, the motion of the center of mass for particles in the lower and upper swarm is analyzed to identify their position when the sudden increase of dispersion is observed. In Fig. 9(a) and (b) we show the time history of vertical and radial trajectories of the centers of mass, made dimensionless using water level, $H$, and tank radius, $R = T/2$, respectively. As already observed, the center of mass of the lower swarm circulates three times along the lower vortex during three impeller revolutions. During the same time, the upper swarm circulates once along the upper vortex. In Fig. 9(c), we show the evolution over time of azimuthal root mean square displacement, $\mathrm{RMSD}_\theta$, of the two swarms, which is used to evaluate the dispersion of fluid parcels.

The $\mathrm{RMSD}_\theta$ of the lower swarm increases significantly only after the third impeller revolution, i.e. when particles transpass the first baffle. Focusing on the $\mathrm{RMSD}_\theta$ of the upper swarm, we observe that dispersion increases sharply just before completing the third revolution, i.e. as soon as the upper swarm is about to complete the first circulation. The location at which the behavior of the azimuthal RMSD changes abruptly is indicated by the arrow in Fig. 9(c). At that point, the position of the center of mass of the upper swarm is identified by the arrow in Fig. 9(a) and (b). Therefore, the reason for such a significant increase of dispersion can be related to the crossing of the region characterized by large strain rates which acts to enhance convective mixing. In particular, the presence of the counter rotating central vortex acts to increase the azimuthal velocity gradient. This phenomenon does not appear in the lower part of the vessel. Observing together in Fig. 7 the snapshot in the third revolution at $\theta = 90°$ and Fig. 8(b), where the arrow indicates the point through which the center of mass of the upper swarm passes, we can pinpoint the position where the center of mass coming from the $v_\theta < 0$ region is crossing the line of $v_\theta = 0$ going toward the $v_\theta > 0$ region. In this region, the space change of the azimuthal velocity determines the strong three-dimensional structure of the upper ring vortex which, in turn, is responsible for the increased dispersion of particles.

In Fig. 9(c), we show for comparison the $\mathrm{RMSD}_\theta$ calculated for two swarms of 3000 particles released within the core of the upper and lower ring vortices. Azimuthal dispersion remains small and almost constant over the number of impeller revolutions for particles released in these regions. Here, the structure of the flow is mainly bi-dimensional and

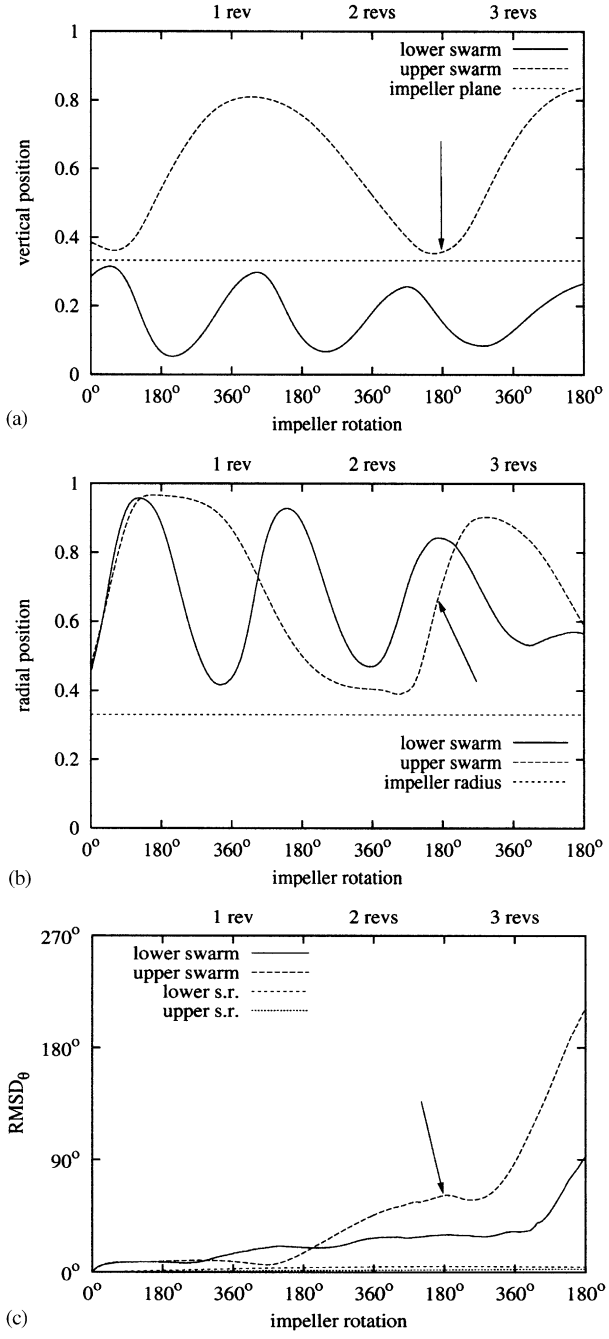


Fig. 9. Vertical (a) and radial (b) trajectory of center of mass of particles released in impeller stream jet and following upper and lower ring vortices. Root mean square displacement of particles in azimuthal direction (c).

azimuthal dispersion is suppressed because the strain rate is everywhere small.

## 4. Discussion and conclusions

In this work, the dispersion of fluid particles in a stirred tank is investigated numerically using a Lagrangian approach. The reactor is the standard vessel configuration (cylindrical tank, four baffles, six-blade Rusthon impeller) experimentally examined by Yianneskis et al. (1987).

The time-dependent, three-dimensional, fully developed flow field in the tank was calculated using a finite volume, RANS code and a $k$–$\varepsilon$ model to simulate the effect of turbulence. A hybrid numerical procedure was devised to reproduce the effect of impeller rotation at best and to limit the computational costs. The accuracy of this procedure was verified—order 2% difference from the full sliding mesh approach—and we calculated computational time savings of up to 67% using the hybrid approach.

The calculated flow field was validated against detailed experiments, finding satisfactory agreement with the LDA data by Yianneskis et al. (1987) and the data by Wu and Patterson (1989), Kemoun et al. (1998) and Michelet et al. (1996), relative to the detailed characterization of the impeller stream jet.

Then, the calculated flow field was used to reconstruct, by a Lagrangian approach, the trajectories of groups of 3000 tracer particles released from different locations in the flow. Circulation length and the circulation time distributions for the tracers were evaluated and we found that mixing proceeds differently in the lower and in the upper part of the tank. We calculated a map for the mean sojour time which was exploited to identify regions of the tank where poor mixing or segregation can be expected.

Finally, we tried to find an explanation for the different dispersion was observed in the lower and in the upper part of the tank. The evolution of particle trajectories released in the impeller stream jet was analyzed in detail and we were able to identify the effects of the large-scale convective structures in the dispersion of particles. In particular, we found a possible reason why fluid tracers behave differently above and below the impeller middle plane. Particles following the downward portion of the blade jet and entrained by the lower ring vortex—a quasi two-dimensional structure—disperse slowly even if they tend to circulate more than once in the vortex. Particles following the upward portion of the blade jet and entrained by the upper ring vortex—a fully three-dimensional structure—disperse fast. Particle dispersion in the upper part of the tank is largely increased by their peculiar path. During the first circulation around the upper ring vortex, particles descend along the impeller axis following the inner counter-rotating vortex and it is when leaving this vortex that particles cross a high strain—highly dispersing—region which contributes to large dispersion values.

## Acknowledgements

Financial support from MURST under grant no. *MM*090314_002 is gratefully acknowledged.

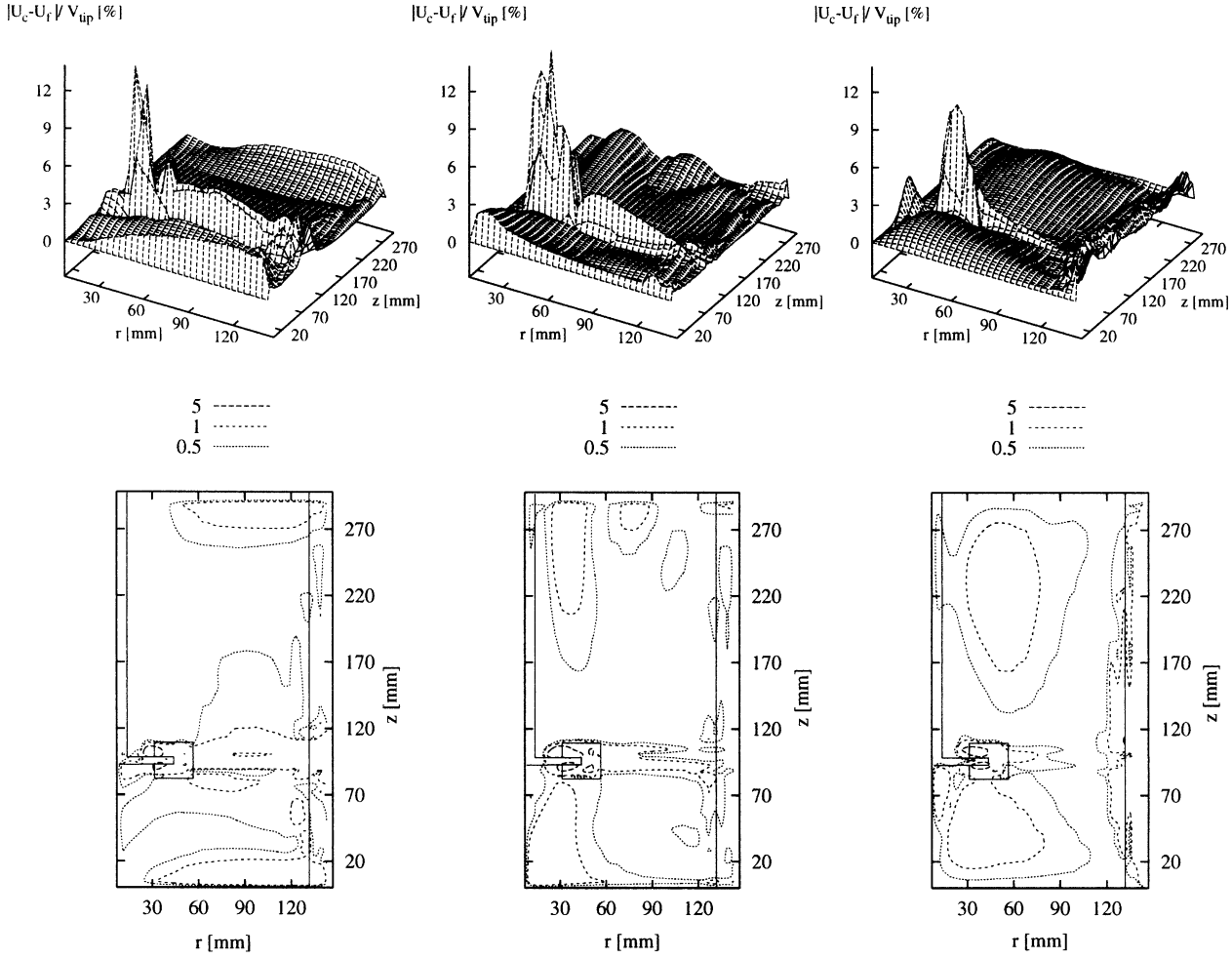


Fig. 10. Difference in radial, azimuthal and vertical components of velocity calculated on coarse and fine mesh models. Difference is normalized to blade tip velocity and is computed on azimuthally averaged flow field.

## Appendix A.

### *A.1. Grid sensitivity analysis*

The determination of the grid resolution is a critical point for Lagrangian simulations: (i) Lagrangian tracking requires interpolation of accurate flow field data; (ii) accurate flow field data are calculated using very fine, nonuniform grids; (iii) the costs for the Eulerian flow field calculation increase linearly with grid resolution; (iv) the costs for interpolation increase more than linearly with the grid resolution for grids which are not regularly arranged in space. Therefore, when selecting the final grid resolution, we tried to find the best compromise between flow field accuracy, computational costs and interpolation costs.

The sensitivity of the simulation to the grid resolution was verified by comparing local values of the flow fields calculated on the coarse, fine and very fine mesh models.

We calculated the flow field for each refined geometry sequentially. We used the pseudo-steady state results obtained on the coarse grid to generate the fine mesh model, refining selectively the mesh in the regions where the gradient of velocity was greater than a threshold value—i.e. in the impeller region and in the near-wall region. We performed a SMA simulation on the fine mesh starting from the already calculated flow field until convergence to the new, grid-dependent, pseudo-steady state was achieved. Monitoring the variation of the power input and the kinetic energy, we found that the new pseudo-steady state was attained after two revolutions. Then, we used the pseudo-steady state flow field obtained on the fine grid to generate the very fine model, using the same procedure for refinement and a lower value for the threshold gradient of velocity. We re-started the SMA simulation on the very fine mesh from the already calculated flow field until convergence to the new, grid-dependent, pseudo-steady state.

In Fig. 10, the differences between the flow fields calculated for the coarse and the fine mesh models are shown, considering local differences in velocity, normalized to the blade tip velocity. Calculations are made for the radial,

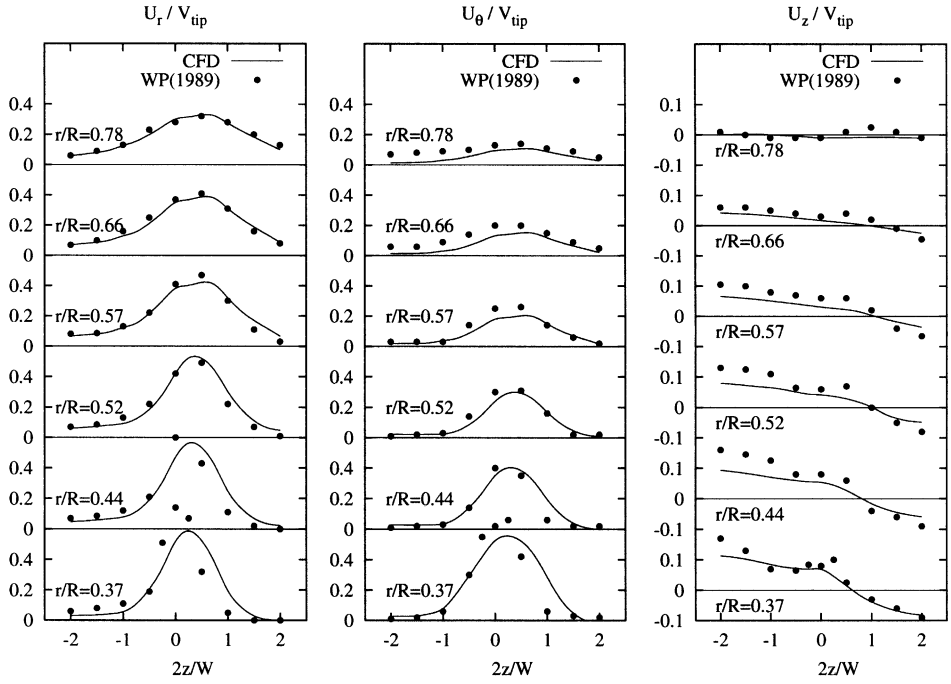


Fig. 11. Mean profiles of radial, azimuthal and vertical component of velocity in impeller stream of Rushton turbine: (●) data by Wu and Patterson (1989), and (–) present numerical simulation.

azimuthal and vertical components of velocity considering different locations in the vertical section of the tank and the azimuthally averaged flow field. The maximum value of the difference is about 14% and is found in the impeller region, where the higher gradients of the velocity field, which are hard to capture with a coarser grid, are successfully resolved by the fine mesh model. In the same way, we assessed the relative improvement in the calculated solution switching from the fine to the very fine mesh model (figure not shown here). We found a local improvement in the solution accuracy lower than 2% everywhere in the vertical section of the tank. Each increase in grid density determines a proportional increase of computational cost for the Eulerian flow field calculation. Nevertheless, this corresponds to a more than linear increase of computational cost for the Lagrangian tracking phase. Therefore, looking for the best compromise between computational accuracy and costs, we assumed that the solution obtained for the fine mesh was grid-independent and sufficiently accurate for the Lagrangian particle tracking.

### A.2. Detailed flow field validation against experiments

We assessed the results of the numerical computation (fine mesh model, 377,432 finite volumes) against the experimental data available from the literature (see the papers by Yianneskis et al., 1987; Wu & Patterson, 1989; Michelet et al., 1997; Kemoun et al., 1998). Experimental data are relative to the structure of the flow field and, particularly, the discharge jet. This structure drives the flow field evolution in the tank and must be simulated accurately to reproduce the flow in the rest of the tank.

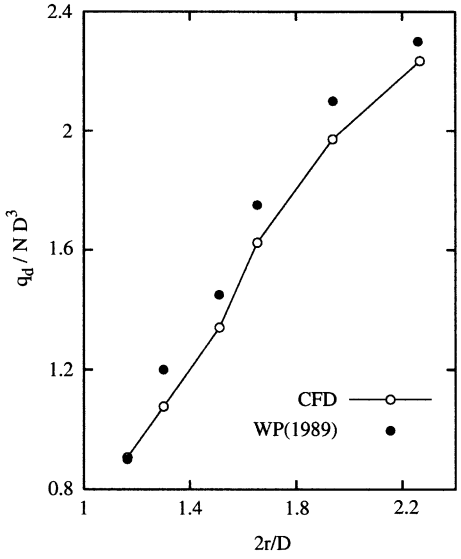


Fig. 12. Profile of radial discharge flow number in impeller stream of Rushton turbine: (●) data by Wu and Patterson (1989), and (○) present numerical simulation.

#### A.2.1. Experiment by Yianneskis et al. (1987)

Yianneskis et al. (1987) used Laser Doppler Anemometry to measure velocity vectors in vertical and horizontal sections of the tank. We compared the calculated flow field with the measurements presented in their paper. The numerical solution reproduces the two ring vortices in the vertical section and the helical vortex behind the baffles. Moreover, in horizontal sections of the vessel velocity vectors show

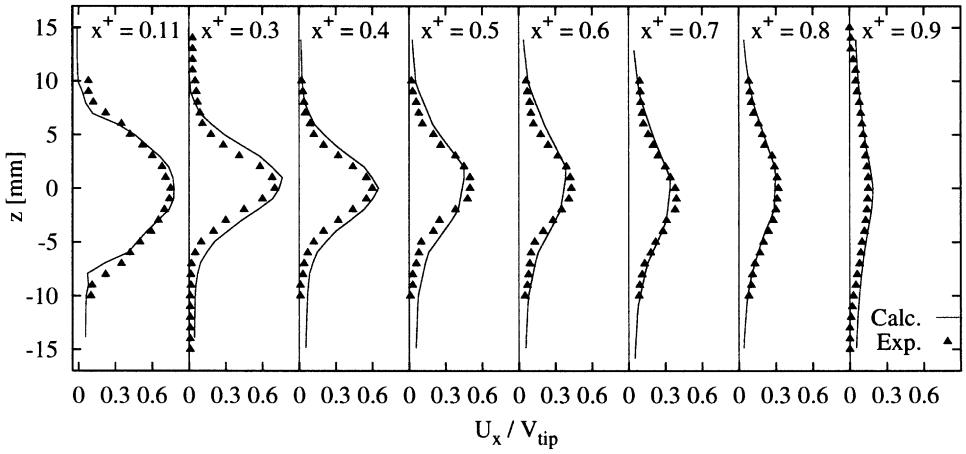


Fig. 13. Comparison with experimental measurements by Kemoun et al. (1998) and Michelet et al. (1997). Vertical profile of theta-averaged velocity along plane tangential to impeller disk for dimensionless radial distances equal to 0.11, 0.3, 0.4, 0.5, 0.6, 0.7, 0.8 and 0.9 $r/R$.

counter rotation of part of the fluid with respect to the impeller. This effect is more evident in the upper part of the vessel, near to the free surface, and is also observable in the lower part. As suggested by Yianneskis et al. (1987), the presence of the baffles reduces the vessel cross-section, generates higher values for the circumferential component of velocity and a reduced pressure, which is balanced by the counter flow. Counter flows are stronger where the circumferential component is lower, i.e. far from the impeller, both near to the bottom of the vessel and near to the free surface. However, the effect of counter flows is different in the upper part of the vessel, where they produce rotation of the upper fluid generating a counter rotating vortex near to the shaft, and in the bottom of the vessel, where they are constrained by the lower wall. The numerical simulation reproduces also the trailing vortices behind the blades, which are quasi-steady structures following the impeller in its rotation.

A more quantitative comparison between simulations and experimental data is shown in Table 2. The simulation predicts the position of the lower and upper recirculating eyes and the upward inclination of the flow around the impeller. However, the calculated power number is underestimated by 12%. The kinetic energy is also underestimated—about 30% in the maximum value and 13% over the volume of the tank—and the dissipation rate is overestimated in the maximum value (near to the impeller) and underestimated elsewhere (Yianneskis et al., 1987; Wu & Patterson, 1989).

### *A.2.2. Comparison against experiment by Wu and Patterson (1989)*

LDA data by Wu and Patterson (1989) were used to assess quantitatively the calculated flow field. Data are radial, azimuthal and vertical components of velocity taken at different radial distances in a $T = 270$ mm vessel and for the impeller rotating at $\Omega = 200$ rpm. Geometrical similarity and fully turbulent flow conditions allow to compare directly experimental and numerical profiles of velocity normalized by the blade tip velocity, as shown in Fig. 11. The three columns in Fig. 11 represent radial (left), azimuthal (center) and vertical velocity profiles (right) taken at different radial distances in the impeller stream ($r/R \geqslant 0.37$). The overall agreement is satisfactory. The main differences between experiment and calculation are for the radial component of velocity at $r/R = 0.37$ ($-20\%$) and $r/R = 0.44$ ($+20\%$). For the vertical component, the largest difference is again near the impeller ($r/R = 0.37$, 0.44 and 0.57), with velocity underestimated by 5% at maximum in the region below the impeller middle plane.

We considered the radial variation of the discharge flow number presented by Wu and Patterson (1989) for further comparison. In Fig. 12, the values of discharge flow computed by our simulation and those presented by Wu and Patterson (1989) are compared. We calculated the discharge flow, $q_d$, integrating over cylindrical surfaces around the impeller the outward directed radial component of velocity. Each experimental point corresponds to a fixed radial position of the cylindrical surface. The calculated discharge flow number, $N_{qd} = q_d/ND^3$, matches closely the experimental value, both near the impeller and in the wall region. This indicates that the development of the discharge jet is well simulated in the different regions of the tank.

### *A.2.3. Comparison against experiment by Michelet et al. (1997) and Kemoun et al. (1998)*

We compared our simulation against the measurements by Michelet et al. (1997) and Kemoun et al. (1998), who used LDA to characterize the turbulent flow field along the impeller stream of a Rushton turbine. They measured the components of velocity in a vertical plane tangential to the impeller disk, and containing the impeller stream jet. Geometrical similarity and fully turbulent flow conditions again allow to compare directly velocity made dimensionless using the blade tip velocity, $V_{tip}$.

In Fig. 13, experimental and numerical velocity profiles from the impeller to the wall of the tank are compared.

Lines and symbols represent simulations and experiments by Kemoun et al. (1998) ($x^+ = 0.11$) and by Michelet et al. (1997) ($x^+ \geqslant 0.3$), respectively. The agreement between experimental data and computation is completely satisfactory.

## References


Bartels, C., Breuer, M., & Durst, F. (2000). Comparison between direct numerical simulation and $k$–$\varepsilon$ prediction of the flow in a vessel stirred by a Rushton turbine. *Proceedings of the 10th European Conference on Mixing*, Delft, The Netherlands (pp. 239–243).

Brucato, A., Ciofalo, M., Grisafi, F., & Tocco, R. (2000). On the simulation of stirred tank reactors via computational fluid dynamics. *Chemical Engineering Science*, *55*, 291–302.

Campolo, M., Fornasier, M., & Soldati, A. (2002a). Modeling turbulent particle dispersion in transverse jets. *Modeling, manipulation and control of transverse jet*. Wien: Springer-Verlag.

Campolo, M., Paglianti, A., & Soldati, A. (2002b). Fluid dynamic efficiency and scale-up of a retreated blade impeller CSTR. *Industrial and Engineering Chemistry Research*, *41*, 164–172.

Campolo, M., & Soldati, A. (2002). Appraisal of fluid dynamic efficiency of retreated blade and turbofoil impellers in industrial size CSTRs. *Industrial and Engineering Chemistry Research*, *41*, 1370–1377.

Delaplace, G., Leuliet, J. C., & Relandeau, V. (2000). Circulation and mixing times for helical ribbon impellers. Review and experiments. *Experimental Fluids*, *28*, 170–182.

De La Villeon, J., Bertrand, F., Tanguy, P. A., Labrie, R., Bousquet, J., & Lebouvier, D. (1998). Numerical investigation of mixing efficiency of helical ribbons. *A.I.Ch.E. Journal*, *44*, 972–977.

Distelhoff, M. F. W., & Marquis, A. J. (2000). Scalar mixing in the vicinity of two disk turbines and two pitched blade impellers. *Chemical Engineering Science*, *55*, 1905–1920.

Fangary, Y. S., Barigou, M., Seville, J. P. K., & Parker, D. J. (2000). Fluid trajectories in a stirred vessel of non-newtonian liquid using positron emission particle tracking. *Chemical Engineering Science*, *55*, 5969–5979.

Gosman, A. D., Ioannides, E. (1981). Aspects of computer simulation of liquid-fuelled combustors. *Paper AIAA-81-0323, presented at AIAA 19th aerospace sciences meeting*, St. Louis, MO.

Graham, D. I., & James, P. W. (1996). Turbulent dispersion of particles using eddy interaction models. *International Journal of Multiphase Flow*, *22*, 157–175.

Guillard, F., Trägårdh, C., & Fuchs, L. (2000). A study of turbulent mixing in a turbine-agitated tank using a fluorescence technique. *Experimental Fluids*, *28*, 225–235.

Harvey, A. D., & Rogers, S. E. (1996). Steady and unsteady computation of impeller stirred reactor. *AIChE Journal*, *42*, 2701–2712.

Harvey III, A. D., West, D. H., & Tufillaro, N. B. (2000). Evaluation of laminar mixing in stirred tanks using a discrete-time particle-mapping procedure. *Chemical Engineering Science*, *55*, 667–684.

Hill, D. F., Sharp, K. V., & Adrian, R. J. (2000). Stereoscopic particle image velocimetry measurements of the flow around a Rushton turbine. *Experimental Fluids*, *29*, 478–485.

Holmes, D. B., Voncken, R. M., & Dekker, J. A. (1964). Fluid flow in turbine-stirred, baffled tank—I: Circulation time. *Chemical Engineering Science*, *19*, 201–208.

Houcine, I., Vivier, H., Plasari, E., David, R., & Villermaux, J. (1996). Planar laser induced fluorescence technique for measurements of concentration fields in continuous stirred tank reactors. *Experimental Fluids*, *22*, 95–102.

Joshi, J. B., Pandit, A. B., & Sharma, M. M. (1982). Mechanically agitated gas–liquid reactors. *Chemical Engineering Science*, *37*, 813–844.

Kemoun, A., Lusseyran, F., Mallet, J., & Mahouast, M. (1998). Experimental scanning for simplifying the model of a stirred-tank flow. *Experimental Fluids*, *25*, 23–36.

Kresta, S. M., & Wood, P. E. (1993). The mean flow field produced by a 45° pitched blade turbine: Changes in the circulation pattern due to off bottom clearance. *Canadian Journal of Chemical Engineering*, *71*, 42–53.

Lamberto, D. J., Alvarez, M. M., & Muzzio, F. J. (1999). Experimental and computational investigation of the laminar flow structure in a stirre tank. *Chemical Engineering Science*, *54*, 919–942.

Lamberto, D. J., Alvarez, M. M., & Muzzio, F. J. (2001). Computational analysis of regular and chaotic mixing in a stirred tank reactor. *Chemical Engineering Science*, *56*, 4887–4899.

Lee, K. C., & Yianneskis, M. (1998). Turbulence properties of the impeller stream of a Rushton turbine. *AIChE*, *44*, 13–24.

Luo, J. Y., Issa, R. I., & Gosman, A. D. (1994). Prediction of impeller-induced flows in mixing vessels using multiple frames of reference. *Transactions of Institute of Chemical Engineers*, *136*, 549–556.

Magni, F., Costes, J., Bertrand, J., & Couderc, J. P. (1990). Structure des ecoulements dans une cuve a fond bombe agitee par une turbine de Rushton. *Canadian Journal of Chemical Engineering*, *68*, 881–892.

Mavros, P., Xuereb, C., & Bertrand, J. (1998). Determination of 3-D flow fields in agitated vessels by laser-doppler velocimetry: Use and interpretation of RMS velocities. *Transactions of Institute of Chemical Engineers*, *76*, 223–233.

McManamey, W. J. A. (1980). Circulation model for batch mixing in agitated, baffled vessel. *Chemical Engineering Research and Design*, *58*, 271–275.

Michelet, S., Kemoun, A., Mallet, J., & Mahouast, M. (1997). Space-time velocity correlations in the impeller stream of a Rushton turbine. *Experimental Fluids*, *23*, 418–426.

Nagata, S. (1975). *Mixing: Principles and applications*. Tokyo, Japan: Kodansha.

Patwardhan, A. W. (2001). Prediction of residence time distribution of stirred reactors. *Chemical Engineering Science*, *40*, 5686–5695.

Patwardhan, A. W., & Joshi, J. B. (1999). Relation between flow pattern and blending in stirred tanks. *Chemical Engineering Science*, *38*, 3131–3143.

Rammohan, A. R., Kemoun, A., Al-Dahhan, M. H., & Dudukovic, M. P. (2001). A Lagrangian description of flows in stirred tanks via computer automated radioactive particle tracking (CARPT). *Chemical Engineering Science*, *56*, 2629–2639.

Ranade, V. V., Joshi, J. B., & Marathe, A. G. (1989). Flow generated by pitched blade turbines, II: Simulation using $k$–$\varepsilon$ model. *Chemical Engineering Communications*, *81*, 225–248.

Sahu, A. K., Kumar, P., Patwardhan, A. W., & Joshi, J. B. (1999). CFD modelling and mixing in stirred tanks. *Chemical Engineering Science*, *54*, 2285–2293.

Serra, A., Campolo, M., & Soldati, A. (2001). Time-dependent finite-volume simulation of the turbulent flow in a free-surface CSTR. *Chemical Engineering Science*, *56*, 2715–2720.

Villermaux, J. (1996). Trajectory length distribution (TLD), a novel concept to characterize mixing in flow systems. *Chemical Engineering Science*, *51*, 1939–1946.

Wernersson, E. S., & Trägårdh, C. (2000). Measurements and analysis of high intensity turbulent characteristics in a turbine-agitated tank. *Experimental Fluids*, *28*, 532–545.

Wu, H., & Patterson, G. K. (1989). Laser-doppler measurements of turbulent flow parameters in a stirred mixer. *Chemical Engineering Science*, *44*, 2207–2221.

Yianneskis, M., Popiolek, Z., & Whitelaw, J. H. (1987). An experimental study of the steady and unsteady flow characteristics of stirred reactor. *Journal of Fluid Mechanics*, *175*, 537–555.

Zhou, Q., & Leschziner, M. A. (1999). An improved particle locating algorithm for Eulerian–Lagrangian computations of two-phase flows in general coordinates. *International Journal of Multiphase Flow*, *25*, 813–825.